Graphene assisted III-V layer epitaxy for transferable solar cells

Carlos Macías, Dyhia Tamsaout, Antonella Cavanna, Ali Madouri, Solène Béchu, Laurent Travers, Jean-Christophe Harmand, Stéphane Collin, Andrea Cattoni, Amaury Delamarre

Graphene assisted III-V layer epitaxy for transferable solar cells

Carlos Macías[a,b], Dyhia Tamsaout[b], Antonella Cavanna[b], Ali Madouri[b], Solene Bechu[c], Laurent Travers[b], Jean-Christophe Harmand[b], Stephane Collin[a,b], Andrea Cattoni[a,b], Amaury Delamarre*[a,b]
[a]Institut Photovoltaïque d'Île-de-France (IPVF), 91120 Palaiseau, France , [b]Centre de Nanosciences et Nanotechnologie (C2N), CNRS, Université Paris-Saclay, 91120 Palaiseau, France, [c]Institut Lavoisier de Versailles (ILV), CNRS, Université Paris-Saclay, 78000 Versailles, France.
*amaury.delamarre@c2n.upsaclay.fr

ABSTRACT

Transferable III-V thin films, combined with light trapping structures, present several interests for photovoltaics: cost, material usage and weight reduction, flexible devices… To obtain such films, remote epitaxy consists in growing above a graphene covered III-V substrate, providing detachable mono-crystals. We report the fabrication of large-area graphene/GaAs substrates by a metal-assisted dry transfer with a high yield (>95%), reduced damage to the lattice, negligible doping, and stress relaxation. After the optimization of chemical etching steps, XPS reveals a residue-free surface with low oxidation levels compared to conventional transfers. Nucleation studies using MBE resulted in the formation of microcrystals, with partial alignment with the underlying GaAs(001).

Keywords: 2D Materials, Epitaxial lift-off, Heteroepitaxy, Solar cell.

1. INTRODUCTION

Epitaxial lift-off techniques are essential for III-V solar cells with light trapping architectures and for the integration of III-V top cells with Si by mechanical stacking. The reuse of the GaAs substrates after lifting-off the epilayer without the need of chemical mechanical polishing would potentially make these technologies compatible with terrestrial applications. Remote[1] and pinhole-seeded[2,3] epitaxy using a graphene interlayer are recently discovered methods where the adlayers can grow epitaxially aligned with the substrate. The devices can be mechanically exfoliated due to the weakened interface enabling substrate reuse for subsequent growths. However, the interplay of the different growth modes that provide epitaxy (or not) remains obscure, and robust methods have not been reported so far due to the difficulties related to the graphene transfer.

We fabricated dry-transferred graphene/GaAs templates for epitaxial GaAs growth, where a high transfer yield (>95%) is ensured by aircushion pressing of the graphene/Ni stack on the target surface. Structural characterization by Raman spectroscopy demonstrates no damage to the graphene lattice, negligible unintentional doping, and stress relaxation during the transfer process. After the optimization of the acid-based selective chemical etching, X-ray photoelectron spectroscopy (XPS) reveals a residue-free surface and a low level of interface oxidation compared to conventional wet-transferred graphene. Nucleation studies using molecular beam epitaxy (MBE) resulted 3D GaAs microcrystals with only partial epitaxial alignment with the GaAs substrate. We did not observe evidence of a robust remote epitaxy effect regardless of the level of interface oxide of the starting graphene/GaAs. These results together with the observed strong degradation of the graphene Raman spectrum at the growth conditions, and the weak remote interaction between the adatoms and the substrate below the graphene in the most ideal situation ($<<K_BT_{growth}$), suggest that pinhole-seeded growth[3] plays a major role on transferring the crystallographic alignment across the graphene. Moreover, when defects are controllably introduced ex-situ to form pinhole seeds, three-dimensional growth of epitaxial islands occurs leading to the formation of a coalesced, mostly epitaxial films with fewer misoriented grains. Pinhole-seeded epitaxy may be an alternative to remote epitaxy and become a potential candidate for low-cost epitaxial lift-off.

2. EXPERIMENTAL

2.1 Graphene growth and transfer

We grow single layer graphene on undoped epi-ready Ge(110) wafers (University wafers) by CVD in an Aixtron BM

vertical showerhead reactor for 3600 s at 930°C[4] with CH_4/H_2 flow ratio of 0.15. To exfoliate the grown graphene, we use a highly stressed Ni film deposited by e-beam evaporation at room temperature. We calculate the film thickness to obtain a stored elastic energy close to ~90% of the reported Ge(110)-graphene work of adhesion[5,6], assuming the internal stress values measured by the Stoney's approach. Prior to the transfer, we dip the semi-insulating (SI) GaAs wafers ((100) surface planes, AXT) in concentrated HCl to remove the native oxides and rinse in different baths of isopropyl alcohol. The stack is later transferred to the GaAs target substrate by aircushion pressing (Nanonex NX2500) at 90°C and an applied pressure of 0.69 MPa, using a thermal release tape (TRT) (Nitto Revalpha 3400MS) temporary substrate. We then chemically etch the Ni layer with a two-step process in Transene etchant TFG and HCl(aq) (37%).

Graphene grown on polycrystalline Cu foils was purchased from Graphenea and transferred with the PMMA-assisted technique[7], using ammonium persulfate 0.3M as the Cu etchant and methyl-isobutyl ketone as the PMMA solvent.

2.2 GaAs growth

Before the introduction in the MBE chamber (Riber 32) we anneal the graphene/GaAs substrates under Ar/H_2 at 500°C to reduce residual oxides and polymeric impurities. The samples are later deoxidized at 620 – 630 °C in ultrahigh vacuum (UHV) under As_2 flux before the growth. We use a growth rate of 0.67 ML/s and a V/III ratio >11 calibrated by Reflection High-Energy Electron diffraction (RHEED) intensity oscillations. Growth experiments were followed in-situ with RHEED.

2.3 Characterization

We use Raman spectroscopy to ascertain the graphene transfer and assess the structural quality using a Renishaw InVia confocal µ-Raman setup with a 532 nm laser excitation source, a 1800 l/mm diffraction grating and a 100x objective (NA=0.85) operated at 0.72 mW. SEM images were taken with a Magellan 400L and analyzed with the ImageJ software. For XPS measurements, we use a Thermo Scientific K-Alpha photoelectron spectrometer with a monochromatic Al K_α source (hv=1486.6 eV) and charge compensation on SI-GaAs substrates. Data were processed using the Thermo Fisher Scientific Avantage© data system.

3. RESULTS AND DISCUSSION

Fig. 1 shows the microscopic and structural characterization of wet (a, b, e) and dry (c, d, e) transferred graphene on GaAs. PMMA residues can be observed in the SEM image of wet transferred graphene (fig 1b) as bright spots because chemisorption of PMMA chains hinders total dissolution of the sacrificial layer. Wrinkles and adlayers are also intrinsic limitations of wet transferred CVD graphene grown on Cu, and observable in fig. 1b. Dry transferred graphene solves this limitations, as shown in fig. 1 c,d, where pinhole defects are the only observed feature (bright spots in fig 1d). Transversal cracks also appear induced by cracking of the Ni layer due to the tensile stress imposed during the exfoliation, spaced by ~1 mm stripes of continuous graphene. However, after the exfoliation of the graphene with Ni/TRT, an intimate contact between the graphene and the target substrate is necessary to achieve a sufficient adhesion over large surfaces to withstand the TRT removal and further processing without lifting-off the graphene. We introduced the use of aircushion pressing[8] to enhance the surface yield of the Ni-assisted dry transfer process. This allows an adequate degassing of the interface by applying a vacuum step and subsequently an ultra-uniform pressure by compressed air on flexible membranes and enables transfer yields (ratio between transferred and initial surface) over 95% reproducibly obtained at the cm^2 scale. The Raman spectrums shown in fig. 1c verify the transfer and provide information on the quality of the graphene layers. The appearance of the momentum conservation-forbidden D band indicates the presence of structural defects in the graphene layer. As the I_D/I_G intensity ratio of the transferred samples does not increase significantly with respect to the as-grown samples neither for the dry transfer ($I_D/I_G \approx 0.16$ vs. $(I_D/I_G)_0 \approx 0.14$), nor for the wet transfer ($I_D/I_G \approx 0.12$ vs. $(I_D/I_G)_0 \approx 0.12$), we conclude that the transfer process is not introducing additional defects. Peak shifts are visible between the as-grown and transferred graphene spectrums. Vector decomposition of the 2D and G frequencies into contributions of mechanical strain and carrier density as proposed by Lee et al.[9] suggest that the dry transfer allows relaxation of the compressive strain in the graphene layer (from between -0.5% and -0.7% to between -0.2% and -0.4%) and does not introduce unintentional doping. An opposite shift observed for both the 2D and G peaks in wet transferred graphene can be explained by a slight increase in compressive strain from ~0.1% tensile to ~-0.3 compressive.

Dry and wet transfer processes have a different impact on the surface chemistry of graphene/GaAs heterostructures, as demonstrated by XPS. Fig. 2 shows the high-resolution spectrums of C 1s, As 3d and Ga 3d photoemission lines. Hydroxyl (285.7 eV) and carboxyl (289.1 eV) are needed for a complete fit of C 1s in wet transferred graphene, possibly enhanced

by the presence of PMMA residues. On the other hand, dry transferred graphene only shows the asymmetric sp^2-like contribution from the graphene. Oxide-related peaks also appear in the As 3d and Ga 3d lines (~9 nm information depth) of the wet-transferred sample (mainly As_2O_3 and Ga_2O_3, respectively). On the dry transferred sample, the graphene is brought in contact with the substrate in a dry environment and protects the deoxidized GaAs surface during further processing steps and air exposure; therefore, As_2O_3 and Ga_2O_3 contributions remain low (1.3 at.%). Importantly, the Ni 2p peak does not appear in the spectrums, indicating a successful etching by our double step process. However, elemental As contributions are evident in the As 3d peak of the dry-transferred sample (5.6 at.%), which decrease the overall Ga/As ratio measured from the 3d levels to 0.72 (0.88 without oxide). As^0 enrichment is a consequence of HCl deoxidation and can be desorbed at relatively low temperature[10]. These differences disappeared after the deoxidation step at 620°C under As_2, that leads to similar levels of oxide and a V/III ratio of 0.96 in both samples.

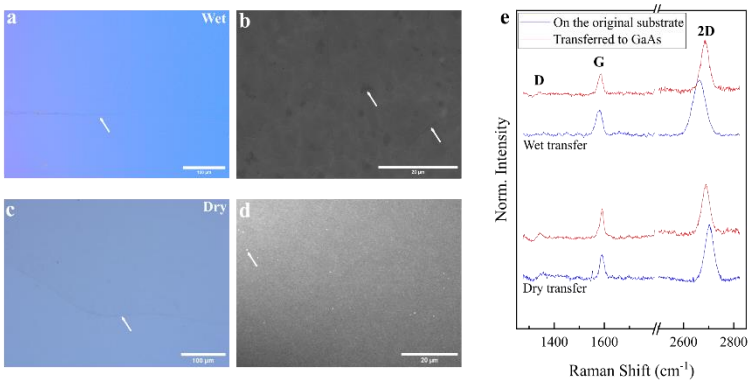

Figure 1: Characterization of the fabricated graphene/GaAs substrates. a, b) Optical and SEM images of dry-transferred graphene/GaAs. The arrows in a, c highlight the weakly visible edge between graphene-covered and uncovered regions, while the arrows in b, d point to the defects discussed in the text. c) Raman spectrums of dry- and wet-transferred graphene/GaAs, before (blue) and after (red) the transfer, that confirm a damage-less transfer in both cases.

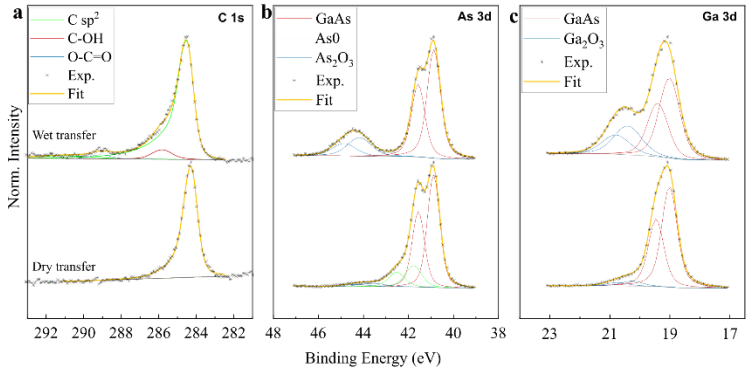

Figure 2: High resolution XPS spectra of C 1s (d), As 3d (e) and Ga 3d of dry- (bottom) and wet-transferred (top) graphene, showing a higher level of oxidation on substrates that undergo the wet process.

Let us now discuss the growth of GaAs on the fabricated graphene/GaAs templates. The results after the growth of 20 GaAs monolayers (ML) are shown in fig. 3. In all the studied cases, nucleation of GaAs proceeds in a 3D growth mode, favored by the relatively low surface energy of the graphene. Comparing fig. 3a and d, and the associated histograms in fig. 3g, one finds that the differences between wet- and dry-transferred graphene are negligible, with almost equal values of island density and average size. Moreover, most of the islands shown in fig. 3a, b (representative of each sample) are growing with non-epitaxial crystal orientations. Only on reduced regions of the samples, the islands grow aligned with the substrate, elongated towards the in-plane [110] directions as shown in fig. 3b, d. These results clearly indicate that neither remote nor pinhole-seeded epitaxy are the dominant growth mechanisms here. In an attempt to observe remote epitaxy, we performed the same growth at lower temperature (450°C). This exponentially reduces diffusion and desorption rates, which hinders the migration of adatoms to pinholes, impurities and topological defects (preferential nucleation sites) and

should favor nucleation on clean graphene regions where remote electrostatic interactions may be strong enough to impose an epitaxial orientation to the growing islands. We observe an improved wetting of the graphene/GaAs surface with a 10-fold increase in island density. However, the orientation of the islands is still mostly non-epitaxial. In-situ RHEED measurements showed Debye rings in the three cases, confirming the polycrystallinity of the deposits. Finally, we observe the growth of GaAs islands on suspended graphene over a trench in the substrate as shown in fig 3f. We find very similar island density and morphology on suspended graphene and GaAs-supported graphene, which shows that the effect of the substrate in these conditions is weak compared to other driving forces.

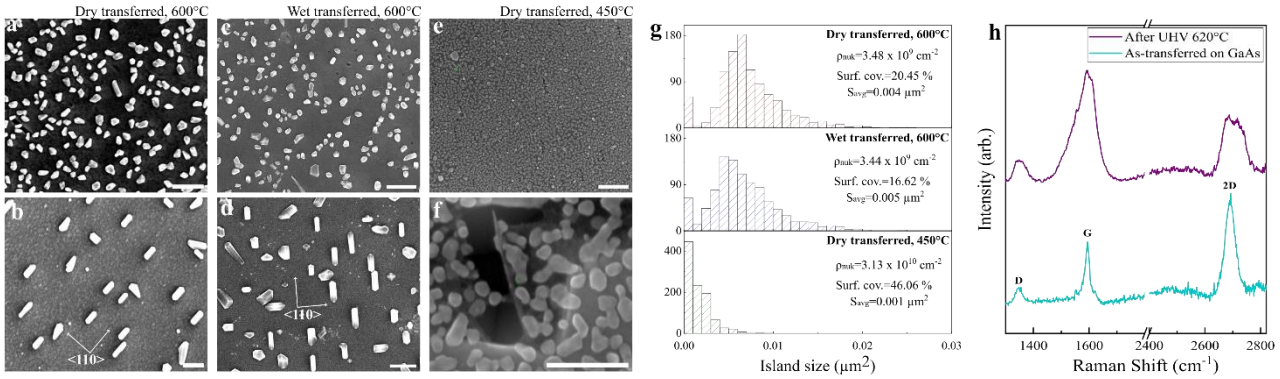

Figure 3: Growth of GaAs islands on graphene/GaAs. a – f) 20 ML of GaAs grown on dry transferred graphene at 600°C (a, b), wet transferred graphene at 600°C (c, d), and dry transferred graphene at 450°C (e, f). The images a, c, e are representative of each sample. The scale bar is 500 nm in the top row and 200 nm in the bottom row. g) Histograms of island sizes from the three samples shown in a – f. The values of the island density (ρ_{nuk}), surface coverage and average island size (S_{avg}) are given in the insets. h) Raman spectrum of the main modes of the graphene before and after the growth of 20 GaAs monolayers.

At the onset of growth of GaAs on graphene/GaAs, there is an interplay between different nucleation mechanisms including remote epitaxy, pinhole-seeded epitaxy, nucleation at impurities, graphene defects or carbides, and possibly Van der Waals epitaxy. Remote and pinhole seeded epitaxy provide an epitaxial alignment with the substrate and it is provenly complicated to differentiate both experimentally[2,11]. On the other hand, XPS reproducibly showed no Ni or other transfer-related contaminants, nor carbides in the C 1s peak after annealing in UHV or H_2. The amount of amorphous C is also expected to be low. But according to the increase in the relative D-band intensity and the widening of the three Raman bands in fig. 4h, the graphene lattice is strongly affected by MBE conditions. Therefore, we hypothesize that defects in the graphene layer may act as preferential sites for nucleation with non-epitaxial orientations. Moreover, the most thermodynamically stable vacancy-like defects in the graphene lattice have been shown to trap metal adatoms and distort the adsorption energy and diffusion barriers by ~2 eV[12,13], two orders of magnitude stronger than what can be expected for the remote epitaxy effect; for a perfect, unreconstructed GaAs(001) surface plane covered with graphene, the DFT-predicted potential energy oscillation over graphene imposed by the underlying GaAs is weak ($<0.26\ KbT_{growth}$)[2,14].

To selectively nucleate only epitaxial islands, we explored pinhole-seeded epitaxy, as a pathway to overcome the stringent requirements of remote epitaxy. We investigated a simple process to introduce nanoholes in the graphene layer based on indirect exposure to O_2 Reactive Ion Etching (RIE)[15]. To identify the nanohole regime we followed the stage of damage with the exposure time to the O_2 plasma by Raman spectroscopy as shown in fig. 4. Ultimately, if the distances between pinholes are within the diffusion length of Ga adatoms, GaAs should selectively form on the exposed substrate seeds. The different stages during plasma exposure (fig 4e) can be distinguished following the evolution of peak ratios shown in fig. 4b-d[15–17]. First, O is chemisorbed on bridge and on-top sites forming sp^3-like defects that give rise to a quick increase in the D band intensity with a small effect on the D' (intravalley scattering defect-related peak). After 70s the I_D/I_G reaches a maximum where $I_{D'}/I_D$ acquires a value of ~7.5, consistent with the dominance of vacancy-like defects[15,16]. In the following, O adsorbs on the more reactive defect sites introduced previously and forms nanoholes by the simple reaction $C + 2O \rightarrow CO_2$, accompanied by a decrease in the I_D/I_G. The opening of the holes is also identified by a sharp decrease in $I_{D'}/I_D$[17], which then slowly decreases to a value of 3-3.5 consistent with dominant edge-like defects[16].

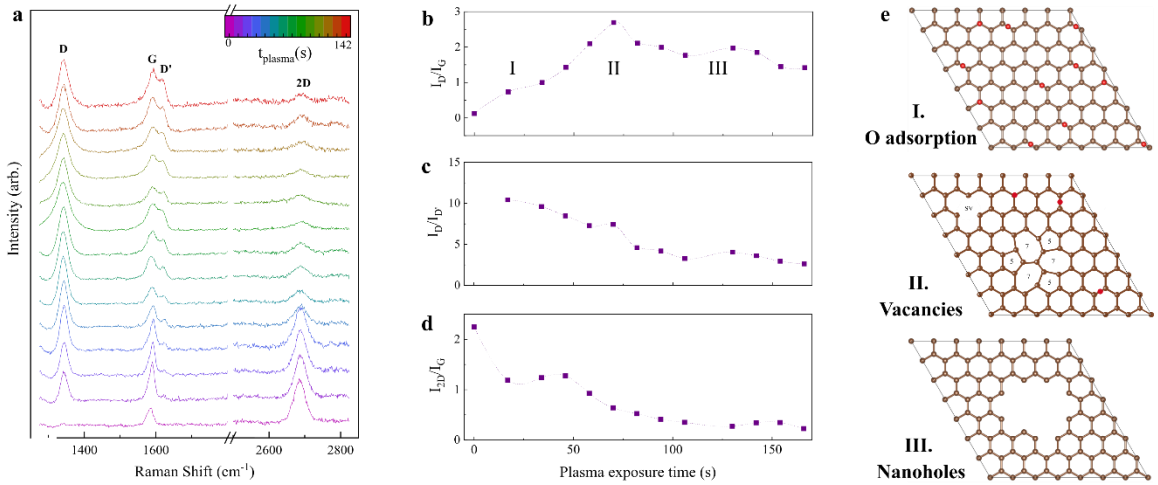

Figure 4: a) Evolution of the Raman spectrum of the GaAs-supported graphene during the exposure to O_2 plasma. b) Schematic representation of the three stages in the formation of a nanohole. These are indicated also in b.

Figure 5a, b show a nominally 250 nm thick GaAs layer grown on unexposed and exposed graphene/GaAs, respectively. The film deposited on unexposed graphene shows a polycrystalline morphology with an average grain size of ~300 nm, consistent with the results shown in fig. 3. On the other side, the film grown on plasma-treated graphene has a faceted surface, apparently with no grain boundaries except the misoriented grains emphasized by the dotted circles. The same facets are recognizable on different spots of the surface, which further suggests that the film is mostly epitaxial, formed by the coalescence of islands with the same orientation. Fig. 5c shows the RHEED patterns at different stages of the growth on exposed graphene. After deoxidation at 630°C a diffuse GaAs (1x1) streak pattern appeared instead of the common c(2x4) surface reconstruction of bare GaAs(100). When the growth starts with Ga deposition, it changes to a spotty GaAs pattern indicating the nucleation of epitaxial islands with no apparent incubation time. At 250 nm, the RHEED is still spotty due to the faceted surface. Weak ring-like features are visible too as highlighted by the red arrows, consistent with the misoriented grains observed by SEM in fig 5b. The θ-2θ XRD pattern of fig. 5d confirms that the dominant out-of-plane direction is aligned with the substrate with (00l) planes parallel to the surface. The surface of the substrate after the exfoliation of the grown layer is shown in fig. e, where spalling marks 10-50 nm wide appear on both directions (into the substrate and into the epilayer), highlighted by arrows, which show that the GaAs layer was directly seeded by the substrate through nanosized openings.

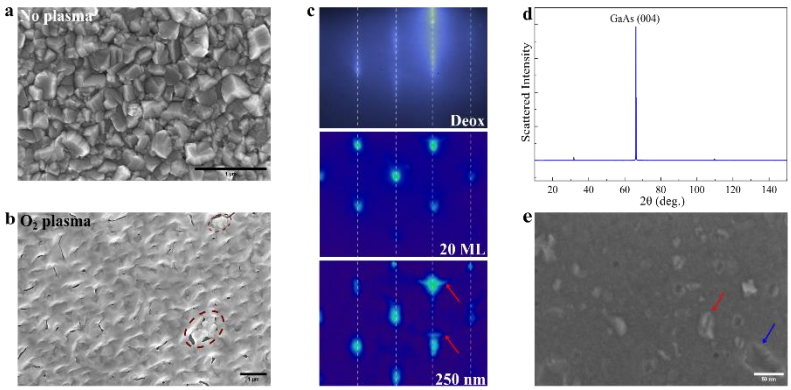

Figure 5: Growth of GaAs on graphene/GaAs exposed to O_2 plasma. a) Growth on unexposed graphene. b) Growth on exposed graphene. c) RHEED patterns of GaAs grown on exposed graphene at different stages of the growth. d) θ-2θ XRD pattern of the layer shown in a. e) Surface of the GaAs substrate after the exfoliation.

4. CONCLUSIONS

We developed a graphene Ni-assisted dry-transfer technique as a platform for experimentation with graphene-assisted epitaxy techniques for two-dimensional material-based III-V layer transfer with photovoltaic applications. The obtained graphene/GaAs heterostructures preserve a high graphene coverage (>95% of the initial graphene surface) enabled by the aircushion pressing technique, without a significant introduction of defects in the graphene lattice and a comparable quality to wet-transferred graphene. The process preserves the surface of the of the underlying GaAs free of oxides and avoids PMMA residues and dopants introduced by the wet route, with only a relative increase of the As^0 contribution related to preferential Ga dissolution during acid treatments.

Despite the differences in surface chemistry between wet- and dry-transferred graphene/GaAs, the surfaces are similar after thermal UHV deoxidation. The first stages of GaAs MBE growth proceed in the same way with randomly oriented nucleation on the graphene being the dominant process, possibly influenced by the degradation of the graphene lattice. A robust remote epitaxy growth is therefore unlikely under standard III-V MBE conditions, given the distortion on relevant energies introduced by unavoidable graphene defects and stress, impurities, etc. However, the orientation of the substrate can be transferred to the growing layer if closely packed pinhole defects are present but still preserve the continuity of the graphene release layer. Optimization of surface planarity and buffer layer growth could lead to defect-engineered graphene as a candidate for the fabrication of low-cost transferrable III-V solar cells on reusable substrates.

ACKNOWLEDGEMENTS

This project has been supported by the French Government in the frame of the program of investment for the future (Programme d'Investissement d'Avenir - ANR-IEED-002-01). The authors acknowledge the French Renatech network.

REFERENCES

1. Kim, Y. *et al.* Remote epitaxy through graphene enables two-dimensional material-based layer transfer. *Nature* **544**, 340–343 (2017).
2. Jang, D. *et al.* Thru-Hole Epitaxy: A Highway for Controllable and Transferable Epitaxial Growth. *Adv. Mater. Interfaces* **2201406**, (2022).
3. Manzo, S. *et al.* Pinhole-seeded lateral epitaxy and exfoliation of GaSb films on graphene-terminated surfaces. *Nat. Commun.* **13**, (2022).
4. Lee, J. H. *et al.* Wafer-scale growth of single-crystal monolayer graphene on reusable hydrogen-terminated germanium. *Science (80-.).* **344**, 286–289 (2014).
5. Yang, S. J. *et al.* All-Dry Transfer of Graphene Film by van der Waals Interactions. *Nano Lett.* **19**, 3590–3596 (2019).
6. Kim, J. *et al.* Layer-resolved graphene transfer via engineered strain layers. *Science (80-.).* **342**, 833–836 (2013).
7. Li, X. *et al.* Transfer of Large-Area Graphene Films for High-Performance Transparent Conductive Electrodes. *Nano Lett.* **9**, 4359–4363 (2009).
8. Gao, H., Tan, H., Zhang, W., Morton, K. & Chou, S. Y. Air Cushion Press for Excellent Uniformity, High Yield, and Fast Nanoimprint Across a 100 mm Field. *Nano Lett.* **6**, 2438–2441 (2006).
9. Lee, J. E., Ahn, G., Shim, J., Lee, Y. S. & Ryu, S. Optical separation of mechanical strain from charge doping in graphene. *Nat. Commun.* **3**, (2012).
10. Liu, Z. *et al.* Preparation of clean GaAs(100) studied by synchrotron radiation photoemission. *J. Vac. Sci. Technol. A Vacuum, Surfaces, Film.* **21**, 212–218 (2003).
11. Du, D. *et al.* Controlling the Balance between Remote, Pinhole, and van der Waals Epitaxy of Heusler Films on Graphene/Sapphire. *Nano Lett.* (2022).
12. Lee, G. *et al.* Diffusion , Coalescence , and Reconstruction of Vacancy Defects in Graphene Layers. *Phys. Rev. Lett.* **95**, 205501 (2005).
13. Cretu, O. *et al.*. Migration and Localization of Metal Atoms on Strained Graphene. *Phys. Rev. Lett.* **105**, 196102 (2010).
14. Kong, W. *et al.* Polarity governs atomic interaction through two-dimensional materials. *Nat. Mater.* **17**, 999–

1004 (2018).
15. Lee, G. *et al.* Precise control of defects in graphene using oxygen plasma. *Journal of Vacuum Science & Technology A* **33**, 060602 (2015).
16. Eckmann, A. *et al.* Probing the nature of defects in graphene by Raman spectroscopy. *Nano Lett.* **12**, 3925–3930 (2012).
17. Jiang, J. *et al.* Modeling Graphene with Nanoholes: Structure and Characterization by Raman Spectroscopy with Consideration for Electron Transport. *J. Phys. Chem. C* **120**, 5371–5383 (2016).